Pergamon

0956-7151(95)00040-2

Acta metall. mater. Vol. 43, No. 9, pp. 3385–3401, 1995
Elsevier Science Ltd

0956-7151/95 $9.50 + 0.00

SPINODAL DECOMPOSITION IN Fe–Cr ALLOYS: EXPERIMENTAL STUDY AT THE ATOMIC LEVEL AND COMPARISON WITH COMPUTER MODELS—I. INTRODUCTION AND METHODOLOGY

M. K. MILLER[1], J. M. HYDE[2], M. G. HETHERINGTON†[2], A. CEREZO[2], G. D. W. SMITH‡[2] and C. M. ELLIOTT[3]

[1]Metals and Ceramics Division, Oak Ridge National Laboratory, Oak Ridge, TN 37831-6376, U.S.A.,
[2]Department of Materials, University of Oxford, Parks Road, Oxford OX1 3PH, England and
[3]School of Mathematical and Physical Sciences, University of Sussex, Falmer, Brighton BN1 9QH, England

(Received 30 November 1994)

Abstract—A three-part series of papers is presented concerning the atomic scale analysis of spinodal decomposition in Fe–Cr alloys. This first part deals with the experimental techniques and computer simulations, the second part discusses the dynamics of early stage phase separation, and the third part describes the morphological and structural characterization of spinodal microstructures. In this first paper, three-dimensional reconstructions of the atomic structure of a series of thermally aged Fe–Cr alloys are shown. Two methods for computer simulation of the decomposition process are described. The first is an atomistic simulation based on the Monte Carlo algorithm and the second is a numerical solution to the Cahn–Hilliard–Cook theory. The three-dimensional atomic scale structures resulting from decomposition within the low temperature miscibility gap are reconstructed. It is shown that both models generate microstructures which are qualitatively similar to those observed experimentally.

1. INTRODUCTION

Many alloys are used under service conditions in which they are metastable or unstable against some form of phase separation on the atomic scale. In a spinodal alloy, there is no thermodynamic barrier to phase separation. During decomposition, the atoms unmix to produce a two-phase microstructure. The Fe–Cr system [1, 2] is an ideal model system for studying the spinodal decomposition process since the lattice mismatch is small (minimizing the effect of lattice strain) and the only competing phase transformation is the sluggish production of sigma phase. Moreover, the reaction is sufficiently slow to permit experimental study of the early stages of phase separation. As decomposition occurs, a highly interconnected microstructure consisting of Fe-rich α and Cr-enriched α' regions is produced, with a characteristic scale (or wavelength) of less than ~ 5 nm.

The conventional theories for spinodal decomposition predict that the phase separation can be divided into two regimes. During the first stage a dominant wavelength forms and the difference in concentration between the two phases is predicted to increase exponentially towards the limits defined by the miscibility gap. On further aging, the sizes of the α and α' regions are expected to increase but the concentrations of the two phases should remain approximately constant. However experimental evidence suggests that both the microstructural scale, and the difference in concentration between the two phases, increase concurrently in the spinodal region of the Fe–Cr system [3, 4].

Several different techniques have been used to characterize the decomposition in spinodal alloys. Recent experimental studies have included the use of X-ray and small angle neutron scattering to measure the structure function [5–9]. As coarsening occurs and the scale increases, there is a decrease in the wavenumber of the peak of the structure function. These reciprocal space techniques are useful for finding average quantities analysing any periodic modulations in terms of Fourier modes. However, no information is obtained concerning the detailed morphology in real space and so a direct comparison with both theoretical models or computer simulations at the atomic scale is impossible. The conventional atom probe field ion microscope [10, 11] has sufficient spatial resolution to directly image the microstructure and is able to collect individual ions whose chemical identity may be determined. Thus local compositions can be calculated on the subnanometer scale. The development of the three-dimensional (3D) atom probes, such as the position-sensitive atom probe (PoSAP) [12–14] and optical atom probe (OAP) [15, 16], enables true 3D characterization of both

†Deceased.
‡To whom all correspondence should be addressed.

composition and microstructure on the atomic scale. Other conventional direct techniques such as transmission electron microscopy have proved ineffective in resolving the fine scale microstructure of the binary Fe–Cr system due to the lack of contrast between the phases.

The high performance of mini-supercomputers now enables sufficiently large 3D simulations of atomic scale processes to yield realistic results. With these tools, numerical simulations and Monte Carlo methods become important techniques for studying phase transitions. Following the emergence of 3D atom probes, it is possible to compare directly the microstructure resulting from fine-scale phase separation with that predicted by theoretical calculations or numerical models. In this series of papers, the phase separation occurring within the low-temperature miscibility gap in a series of Fe–Cr alloys is compared with two models of the decomposition process.

The microstructures have also been related to the observed mechanical properties. The increase in hardness (and decrease of impact strength) during spinodal decomposition is of crucial engineering importance, notably in the duplex stainless steels used in the primary cooling circuits of many nuclear reactors. The time and temperature dependence of the spinodal reaction needs to be understood in order to satisfactorily predict the long-term behavior of these materials.

2. MATERIALS AND HEAT TREATMENTS

The majority of the research reported in this series of papers was performed on a high purity Fe–45 at.% Cr alloy. This composition was chosen to be in the centre of the slightly asymmetrical miscibility gap. This alloy was fabricated from high purity elemental Fe (>99.99% purity) and Cr (>99.996% purity). Chemical analysis of the alloy after arc-melting in a dry argon atmosphere revealed that it contained a total of ~100 ppm of interstitial impurities by weight. Wire, of diameter 0.25 mm, was fabricated from the master ingot by a combination of swaging and wire drawing operations. Special precautions were taken to prevent contamination of the material during these stages. Some additional experiments were performed on Fe–17, 19, 24 and 32 at.% Cr alloys which were fabricated in exactly the same manner from the same initial materials.

Prior to examination in the atom probe, the wires of the Fe–17, 19, 32 and 45% Cr alloys were solution treated in argon (0.4 atm) for 2 h at 1273 K, water quenched and isothermally aged at 773 K for times up to 500 h and water quenched. The Fe–24% Cr alloy was solution treated for 16 h at 1223 K prior to isothermal aging at 773 K. In addition to these 773 K isothermal treatments, a series of isothermal heat treatments at temperatures ranging from 673 to 923 K was performed to estimate the position of the miscibility gap by the experimental observation of phase separation in the field ion images.

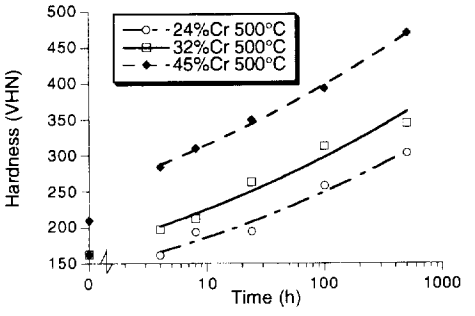

Fig. 1. Hardness vs heat treatment for Fe–Cr alloys containing 24, 32 and 45% Cr (200 g load).

The change in microhardness as a function of aging time at 773 K was determined from the ends of the wires with the use of a Shimadzu hardness tester with a 200 g load. The results are shown in Fig. 1 for the 24, 32 and 45% Cr alloys. The increase in hardness was greatest for the alloys with the highest Cr content, as expected due to the higher volume fraction of the Cr-enriched α' phase. The time exponents of the changes in hardness were determined by fitting each set of data to a power law as indicated by the lines in Fig. 1 and were 0.13 ± 0.02, 0.12 ± 0.01 and 0.10 ± 0.01, respectively for the 24, 32 and 45% Cr alloys.

These microhardness results correlate well with the work performed by Marcinkowski *et al.* [2]. Their room temperature hardness measurements on an Fe–47.8 at.% Cr alloy quenched from 1273 K and aged at 773 K showed that the average hardness doubled with aging before reaching an apparent plateau of 470 VHN after 500 h aging.

3. EXPERIMENTAL TECHNIQUES AND DATA ANALYSIS PROCEDURES

3.1. Atom probe microanalysis

The primary technique used to characterize the microstructures of these alloys was atom probe field ion microscopy (APFIM). A detailed description of this technique may be found in the monograph by Miller and Smith [17]. In order to perform a complete microstructural characterization, both an energy-compensated atom probe and two variants of the newer 3D atom probes were used, a PoSAP and an OAP.

The field ion microscope (FIM) provides an atomic resolution view of the surface of a specimen. Variations in composition often generate phase contrast on the image but no compositional information is available. The FIM images shown in Fig. 2 show the increasing scale of decomposition as a function of aging in a series of Fe–45% Cr alloys. The morphology of the microstructure may be observed by taking a series of field ion micrographs as the specimen is field evaporated to expose new layers of material (i.e. serially sectioned). Field desorption micrographs of

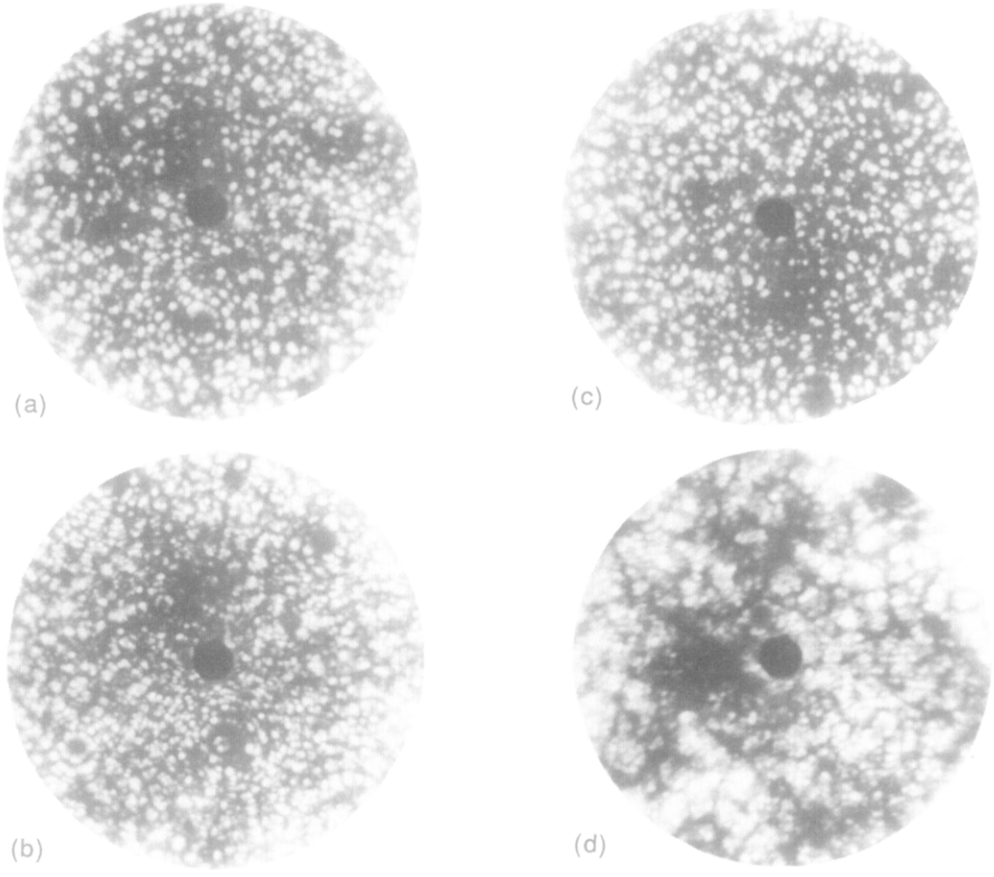

Fig. 2. Field ion micrographs from Fe–45% Cr samples aged for (a) 4, (b) 24, (c) 100 and (d) 500 h. The brightly imaging regions are Cr-enriched and the dark regions Cr-depleted.

the specimen surface, generated by individual field-evaporated ions in the optical atom probe, often show better phase contrast than field ion micrographs. In Fig. 3 a series of field desorption micrographs show how the morphology of phase separated Fe–Cr alloys varies with the Cr content. As the Cr content of the alloy is increased, the volume fraction of the α' phase increases and there is a transition in the morphology of the α' phase from approximately spherical particles [Fig. 3(a)] to a fully interconnected structure [Fig. 3(d)]. Although the 24% Cr alloy appears to consist simply of isolated regions, field evaporation sequences demonstrate that the α' phase forms some interconnected regions and some isolated particles.

In order to obtain compositional information, an atom probe compositional analysis must be performed. Atom probes collect individual ions whose chemical identity can be determined. The local composition can be calculated on the nanometer scale and used to generate a one-dimensional (1D) depth profile. The 3D atom probes can be used to reconstruct elemental maps of the sample in three dimensions with near atomic resolution. Moreover the analyses may be used to determine several additional parameters related to the microstructural scale and elemental concentrations, as described in the following sections and in Parts II and III of this series [18, 19].

3.2. Experimental conditions

The experimental conditions were chosen to suit the type of analysis and therefore varied among each of the techniques used. The field ion micrographs were obtained with the use of neon as the image gas and with a specimen temperature of between 60 and 85 K. The field desorption micrographs were recorded with a specimen temperature of 60 K. All 1D atom probe analyses were obtained with the use of the Oak Ridge National Laboratory energy-compensated atom probe (ECAP) [20] with a specimen temperature of 50 K and a pulse fraction of 20%. In the PoSAP experiments, a relatively high analysis temperature of 80 K was chosen to minimize the loss of information caused by the simultaneous evaporation of more than one Cr atom on a single pulse [21] and a pulse fraction of 15% was used. An ion rate of between 50 and 100 pulses per ion was used as a compromise between minimizing the number of multiple events and maximizing the rate of data acquisition.

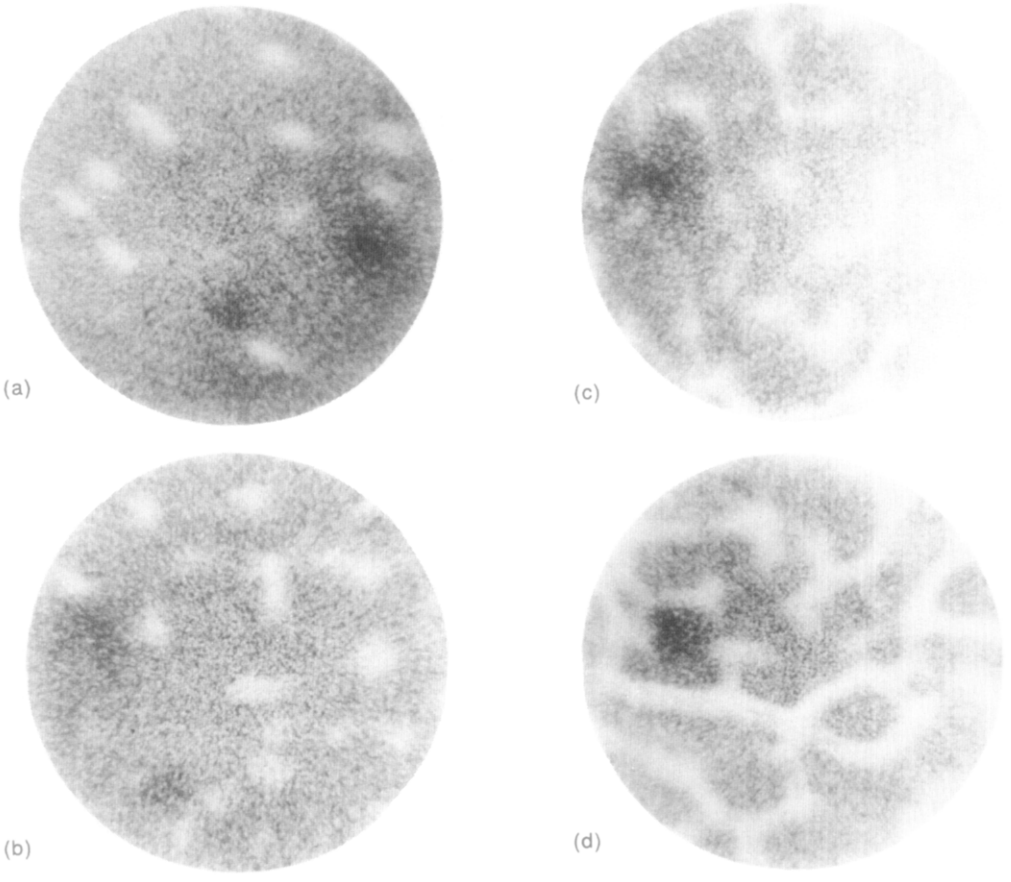

Fig. 3. Field desorption micrographs from Fe–Cr alloys aged for 500 h at 773 K as a function of Cr content—(a) Fe–19% Cr, (b) Fe–24% Cr, (c) Fe–32% Cr and (d) Fe–45% Cr. The bright regions are Cr-enriched and darker regions Cr-depleted.

3.3. Composition profile

On the atomic scale, it is impossible to treat the local composition of an alloy as a continuous variable. A composition must be defined over some local region, called a coarse-graining volume, which is small with respect to the length scales of features of interest, but considerably larger than the size of an atom. A composition profile may be generated by dividing the sequence of ions from an ECAP analysis into blocks and plotting the block composition against block number. The blocks can be chosen so that each has an identical volume or so that each contains a fixed number of atoms. In the former case, local magnification effects will cause different blocks to contain different numbers of ions making statistical analysis difficult. The size of each block is chosen so as not to smooth over the composition fluctuations, but large enough so that most of the statistical noise is excluded. A qualitative examination of a composition profile can be used to detect composition fluctuations. The analysis may be applied to PoSAP data, by selecting a sub-volume, usually in the form of a cylinder of square cross-section, which is then divided into blocks. However, much longer composition profiles are obtained from conventional atom probe analysis because of the greater depth analysed. For isotropic morphologies, the blocks are usually chosen to be approximately cubic, with a size which does not smooth over the composition fluctuations, but is large enough to exclude most of the statistical noise.

ECAP composition profiles through an Fe–45% Cr alloy aged at 500°C for 24 and 500 h are shown in Fig. 4(a, b). Equivalent PoSAP depth composition profiles using a moving average smoothing with a fixed sample volume (1 nm^3) are shown in Fig. 4(c). In the early stages of decomposition small composition fluctuations are evident. At later stages of decomposition, well defined sinusoidal type composition modulations are observed. Note that the observed maximum composition in each vein does not appear constant. This is the natural consequence of simultaneous sampling of both phases, rather than sampling pure Fe-rich regions and pure Cr-enriched regions. An approximate estimate of the wavelength can be made by counting the number of wavelengths traversing the volume. After 24 h the wavelength is

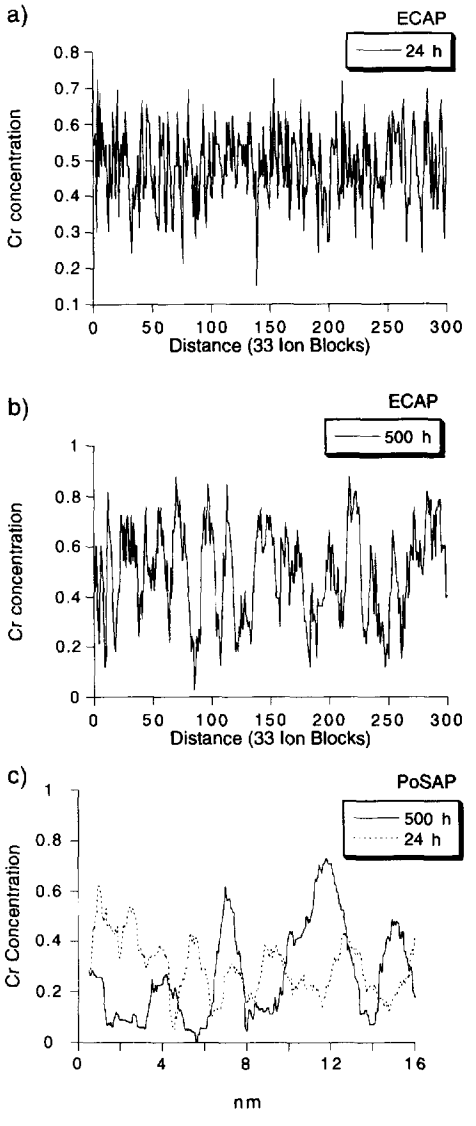

Fig. 4. Composition profiles for two Fe–45%Cr alloys thermally aged for 24 and 500 h. In (a, b), results from an energy compensated atom probe using a constant block size of 33 ions are shown. In (c) data from PoSAP experiments using a constant sample volume of 1 nm^3 is displayed.

approx. 2 nm, and increases to over 4 nm after 500 h. More accurate statistical techniques for analysing the development of microstructural scale are presented in Part II of this series [18]. The increase in domain composition can be more clearly observed by plotting a frequency distribution.

3.4. *Frequency distributions*

A frequency distribution curve from a conventional atom probe experiment is constructed by dividing the sequence of atoms into equal sized blocks of atoms and plotting the observed number of blocks with each composition. A random solid solution will generate a binomial form, whereas a system in which phase separation has occurred will exhibit a broadening of this distribution. In the limiting case, a heavily decomposed sample will yield a distribution with two peaks corresponding to the development of two separate phases. The development of the frequency distribution is shown in Fig. 5 for the Fe–45% Cr alloy aged between 4 and 500 h at 773 K and analysed in an energy-compensated atom probe. At the earliest stages, before significant phase separation has occurred, the distribution follows the binomial form. During aging, the distribution first broadens and, at the latest stages, begins to show two peaks. Methods for quantifying the extent of decomposition based on the form of the frequency distribution are discussed in Part II of this series [18].

3.5. *3D atom probe data representation*

The simplest and most intuitive representation of 3D atom probe data is to use a sphere to represent each individual atom. Different types of atom may be represented by different colours and the use of various forms of shading and lighting conditions can be used to highlight various features. This method has been used in Fig. 6 to show the distribution of Fe and Cr atoms in an Fe–45% Cr specimen after aging for 500 h at 773 K. The lighter-coloured spheres represent Fe atoms and the darker spheres represent Cr atoms. Clearly, thermal aging has generated a two-phase interconnected web consisting of Cr-enriched regions and Fe-rich regions. The figure reveals that each "domain" is only a few nanometers thick.

Since the atoms at the surface of the analysed volume obstruct the line of sight from those atoms in the bulk, it is impossible to visualize the internal structure by the method used in Fig. 6. For complicated morphologies, it is useful to define a regular 3D grid of composition cells, as shown in Fig. 7(a). Each cell is assigned a composition according to the local environment of atoms. The size of an individual cell is close to that of an atomic spacing to ensure that spatial information is not lost. However, this means that each cell contains, on average, only one or two atoms. Since trajectory aberrations occur during field evaporation the original location of each atom cannot be precisely located. This invariably means that many cells will contain no

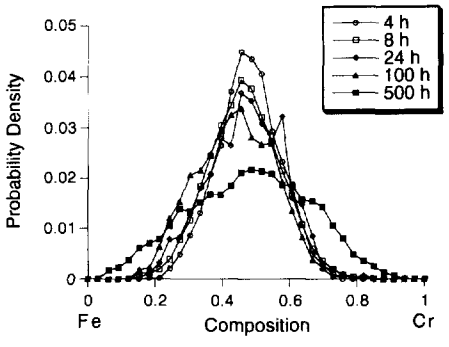

Fig. 5. Frequency distributions from ECAP analyses of a series of Fe–45% Cr alloys aged up to 500 h. A block size of 33 ions was used.

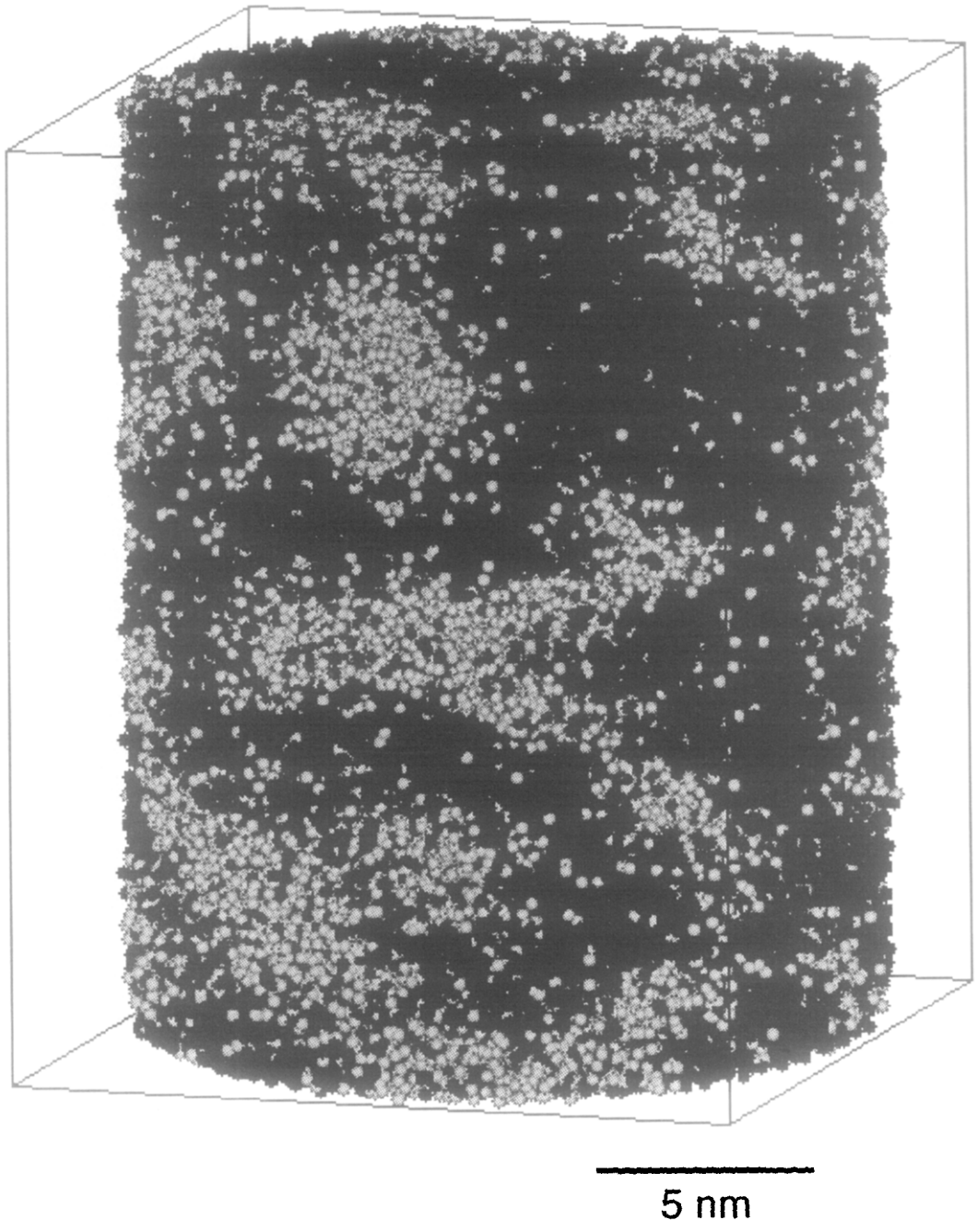

Fig. 6. Atomic reconstruction of an Fe–45% Cr alloy aged for 500 h. The lighter spheres represent Fe atoms and the darker spheres Cr atoms.

atomic information from which a composition may be calculated. Moving average sampling methods must be introduced to ensure that no "holes" remain in the data. Since an average data set will contain at least 200,000 atoms, the algorithm must be extremely efficient.

Two types of sampling are considered. In the first [Fig. 7(b)], all points within the sampling volume contribute equally to the composition calculation (simple smoothing). This will tend to smooth out fine detail present in the structure. The second, centre-weighted, smoothing method is heavily biased towards those atoms nearest to the centre of the smoothing volume [Fig. 7(c)]. This algorithm is essentially a "hole filling" algorithm since it assigns compositions to cells from within which no atoms could be located without significantly affecting the compositions of surrounding cells. The result of this smoothing is a grid containing a higher level of fine detail. The size of the averaging volume is not critical provided that all of the cells may

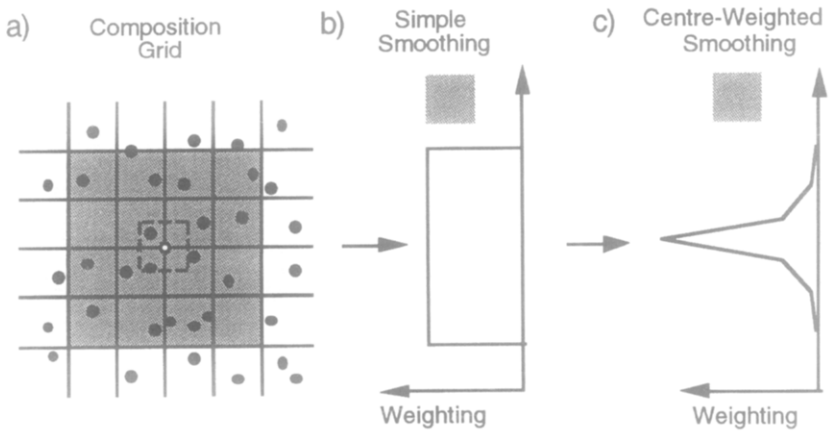

Fig. 7. Principle of composition grid. The grid used to calculate composition is of a similar size to the atomic spacing (a). Individual cells on the grid may have no atom positions within their volume. Moving average smoothing methods are used to ensure all points on the grid have composition data. In simple smoothing (b), atom positions over the shaded area contribute equally to the composition at the grid point, while centre-weighting the data (c) produces a composition biased towards atoms close to the grid location.

be assigned a local composition. Typically a cubic region with side 4 cells (simple smoothing) or 5 cells (centre-weighted smoothing) is used.

For a binary alloy, the compositions can be false-colour coded. The range of colours in the rainbow spectrum can be mapped to the composition values, for instance from blue representing A-rich regions through green to red representing B-rich regions. A series of cross-sections through the structure can be used to represent the 3D morphology and to observe the degree of interconnectivity. A grey-scale equivalent is shown in Fig. 8.

A binary image can be formed by defining a composition threshold. Cells with compositions above and below this threshold are assumed to originate from regions of different phases. The choice of threshold composition is critical since it determines the apparent volume fraction of each phase. The simplest choice for a threshold value is the mean alloy composition. This choice would be suitable for an alloy in which the two phases had concentrations symmetrically positioned on either side of the mean alloy composition. However, if the volume fractions of the two phases were not equal this choice could generate an interface within one of the phases as shown in Fig. 9. In this diagram, two frequency distributions are shown, the first corresponding to an unaged alloy and the second to the late stages of aging after two distinct phases have formed. Both have the same mean composition. Choosing the mean composition to be the threshold level is clearly not suitable. Choosing the threshold level as the composition of the median block could yield a similar result. An alternative choice would be that of the mid-value between the maximum and minimum compositions observed. However this value would be influenced too much by statistical variations at the upper and lower end of the distribution. The method selected attempts to avoid these statistical variations by locating the positions of the upper and lower deciles and using the mid value between the two. As can be seen from Fig. 9, a much better estimate of the true threshold composition is obtained. Several other choices for a threshold value are possible. For instance, if the frequency distribution consists of two distinct peaks, the minimum value between the two peaks could be selected.

3.6. Isosurface reconstruction

The sequence of binary cross-sections can be extended to generate the full 3D microstructure by generating an isosurface, the 3D equivalent of a contour. A composition level is chosen and a surface drawn over all points with this composition. The resulting structures consist of thousands of polygons which can be automatically shaded and manipulated in 3D using visualization software to give a full 3D impression. This technique has proved particularly useful for examining percolated or highly interconnected structures.

An isosurface representation was used to show the atomic scale composition variations found in Fe–Cr specimens after aging at 773 K. A simple smoothing algorithm was used to generate the composition grid. Alloys with a low Cr content phase separate to give microstructures with a low volume fraction of the second phase. The microstructure therefore consists of isolated Cr-enriched particles within an Fe-rich matrix. An example is shown in Fig. 10(a), where an isosurface reconstruction, drawn at a concentration of 20% Cr, has been used to represent the Cr-enriched regions from an Fe–17% Cr alloy aged for 500 h. In Fig. 10(b), the isosurface from an Fe–24% Cr alloy aged for 500 h demonstrates that both isolated particles and veins traversing the analysed volume can co-exist. The Cr-enriched regions of the Fe–32% Cr alloy aged for 500 h form a percolating structure with little evidence for large isolated particles [Fig. 10(c)]. Analyses of the Fe–45% Cr alloys show that after 4 h

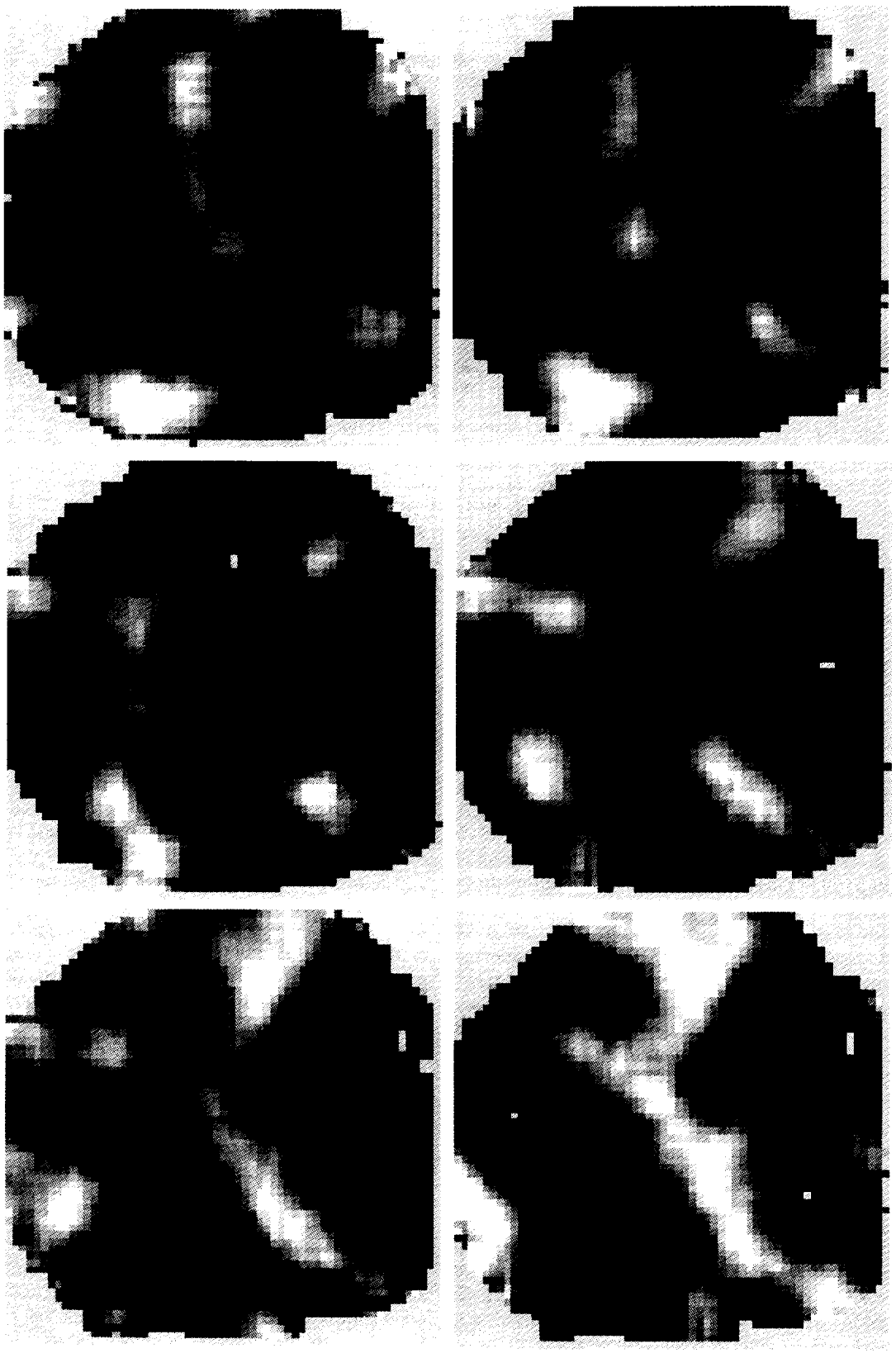

Fig. 8. Series of cross-sections through the structure of an Fe–45% Cr alloy aged for 500 h. The compositions were calculated using simple smoothing. The dark regions are Cr-enriched and the lighter regions Fe-rich. The series represents a depth of approx. 4 nm.

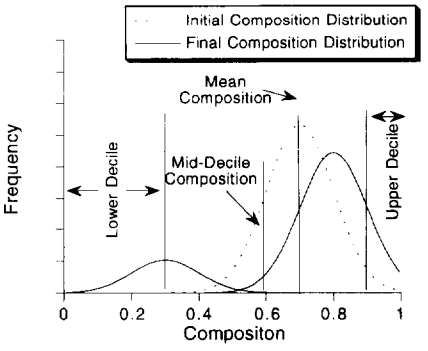

Fig. 9. Broadening of composition frequency distribution during spinodal phase separation. The lower (and upper) deciles mark the composition below (and above) which 10% of the composition values are observed. The threshold composition, which represents the interface between the two phases, is defined as the mid-point between the compositions of the upper and lower deciles.

aging there is little evidence of any decomposition, whereas after 24 h, Cr-enriched veins have begun to form. A highly interconnected two-phase microstructure is found after aging for 100 h. In Fig. 10(d), an isosurface has been drawn to represent the Cr-enriched regions present after aging for 500 h. Figure 10(a–d) can be directly compared with the field desorption micrographs in Fig. 3. In Fig. 10(e) centre-weighted smoothing, which retains a higher level of detail than simple smoothing, has been used to calculate the local composition in an Fe–45% Cr sample after aging for 500 h. Although the phases are well defined, it is apparent that the interface is rough on the atomic scale and that some very small isolated Cr-enriched regions exist. At this stage of decomposition, the domains are approx. 2.5 nm across. In all of these isosurface reconstructions, no preferred growth orientation was detected, consistent with the small strain associated with the system.

4. COMPUTER SIMULATIONS

4.1. Theories for spinodal decomposition

Conventional theories of phase separation have so far been based on Gibbsian thermodynamics. Implicit in the models is the use of a coarse-graining volume large enough for the composition to be treated as a continuous parameter. The coarse-graining volume must therefore be considerably larger than the scale of a lattice site. However, the volume must also be small in comparison with the length scales of the features of interest such as the wavelength of composition fluctuations. A mathematical theory of spinodal decomposition was developed by Cahn and Hilliard [22, 23]. The linear solution explained the growth of composition waves and their crystallographic orientation but was only valid at the very early stages of decomposition. Cook [24] later improved the Cahn–Hilliard model by including a term to model thermal noise. Non-linear theories [25, 26], also based on continuum models, have been developed to describe the growth rate at intermediate and later stages of decomposition but these have met with only limited success, and yield no information on the detailed morphology of the resulting microstructures. In the present work, two models of the decomposition process have been implemented: a discrete atomistic model and a numerical solution to the non-linear Cahn–Hilliard–Cook equation.

4.2. The dynamic Ising model

Phase separation in alloys is generated by diffusion of atoms through the microstructure, and is driven by the reduction of free energy. The Monte Carlo technique can be used to model this process. A Hamiltonian is defined in terms of "pair-wise" bond energies summed over all possible interactions and the change in enthalpy is calculated when a random pair of nearest neighbour atoms is swapped. If only nearest neighbour interactions are considered, the change in energy, ΔH, will be a multiple of the interaction parameter, $\epsilon = E_{AA} + E_{BB} - 2E_{AB}$, where E_{AA}, E_{BB} and E_{AB} are the energies associated with a A–A, B–B and A–B interactions respectively. The probability $P(x \rightarrow x')$ that the new lattice configuration is accepted is given by the Metropolis algorithm [27] and the change in energy ΔH

$$P(x \rightarrow x') = \begin{cases} \exp[-\Delta H/kT] & \Delta H > 0 \\ 1 & \Delta H \leq 0 \end{cases}$$

The algorithm is not designed to simulate exact microscopic behaviour. For this, a pre-factor in the form of $(A/\tau)\exp[-Q/kT]$ is necessary where Q is the activation energy, A a positive constant and $1/\tau$ the attempt frequency. This would simulate the lattice vibration process but would also necessitate a large number of attempts (determined by the magnitude of Q) before a swap actually occurs. In the case where the diffusion barrier is assumed constant, the algorithm is a good simplifying model. Clearly, in real systems, Q will be a function of the local atomic configuration. If the pre-exponential term is the same for both species, this term simply scales the time, and so it can be ignored.

Vacancy diffusion can be modelled by allowing a "hole" in the lattice to execute a random walk. In this situation the energies of "bonds" between the vacancy and surrounding atoms need to be defined. The simplest method is to define the A–vacancy "bond" and B–vacancy "bond" energies as being equal so that no preferential segregation of vacancies to any single phase occurs. If only a single vacancy is allowed, then a vacancy–vacancy interaction does not need to be defined. Simulations using a vacancy mechanism have given very similar results to the "unphysical" nearest neighbour swapping technique [28]. For simplicity, all simulations reported here used the atom swap technique.

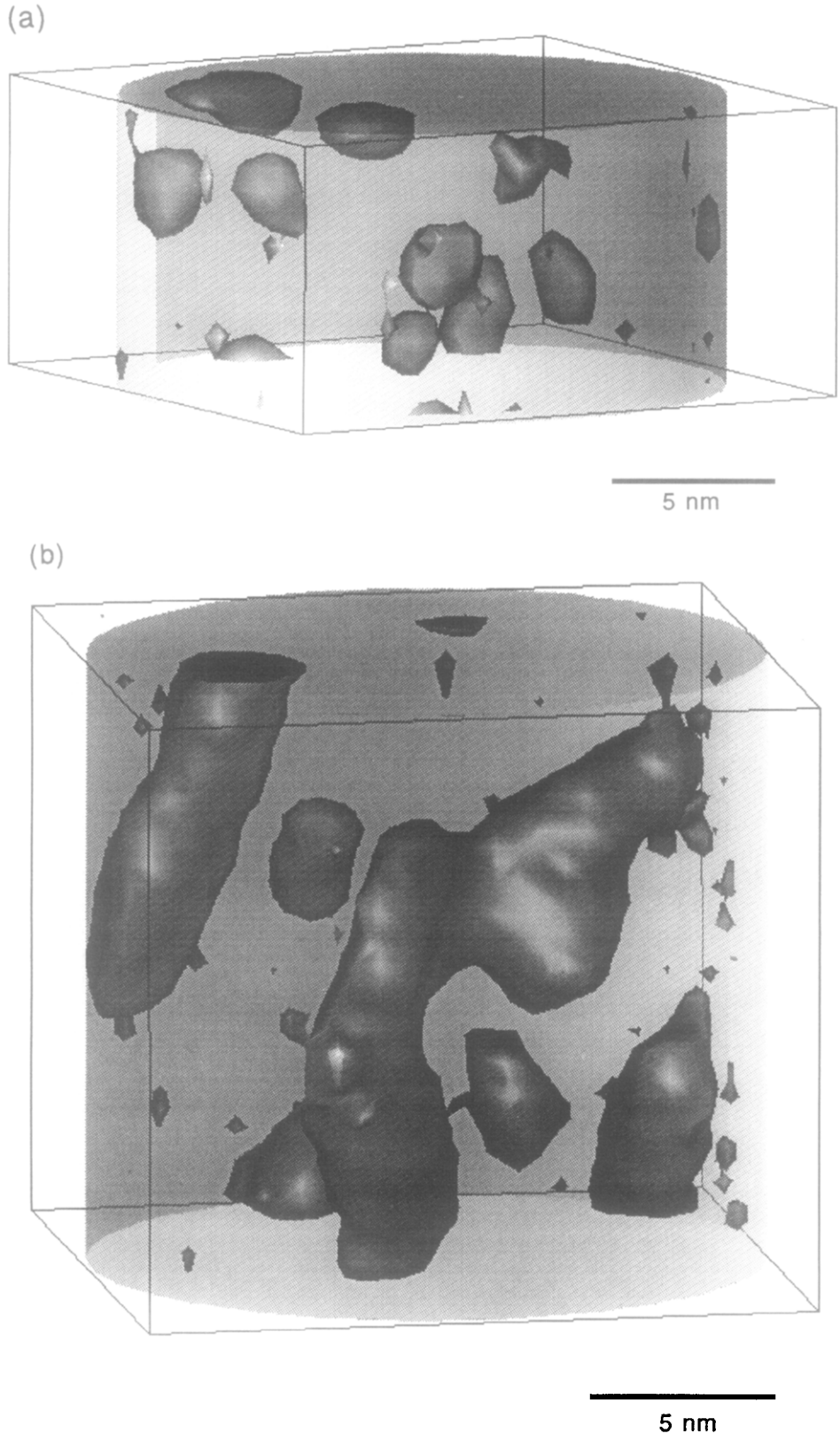

Fig. 10(a–b). (*Caption on p.* 3397.)

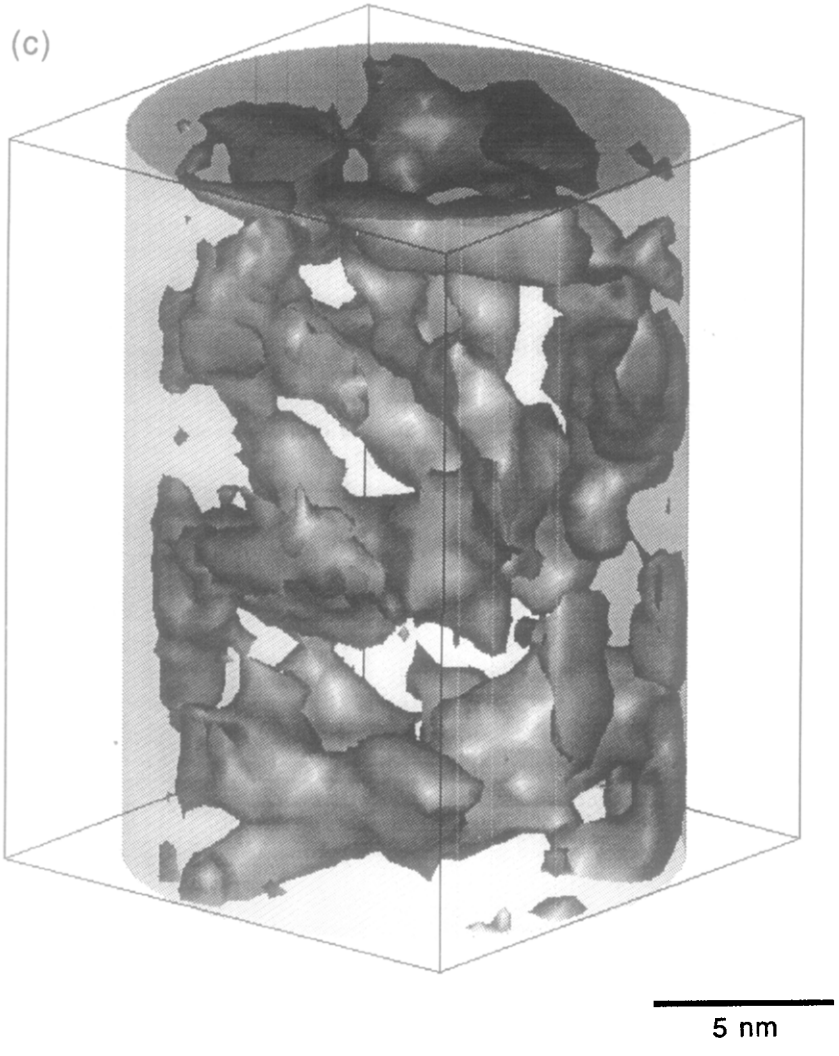

Fig. 10(c). (*Caption on p.* 3397.)

In the case of a b.c.c. lattice (such as the Fe–Cr system), simply using nearest neighbour interactions to calculate the enthalpy associated with a lattice site is clearly not realistic, since the six second nearest neighbours are not much further away than the eight nearest neighbours and therefore poorly screened. Second nearest neighbour interactions must also be used, and weighted according to how the interatomic potentials vary as a function of distance (s). In the $3d$ transition metals, the binding potential falls approximately as s^5 [29].

The nearest neighbours are situated at a distance $(a_0\sqrt{3})/2$, where a_0 is the lattice parameter. The second nearest neighbours are situated at a distance a apart. The weighting is therefore given by

$$\left(\frac{\sqrt{3}a_0/2}{a_0}\right)^5 \approx \frac{1}{2}.$$

For a simple or f.c.c. lattice, an algorithm using only nearest neighbour interactions is sufficient. Time in the Monte Carlo model is defined in terms of Monte Carlo steps (MCS). If there are N atoms in the simulation then one MCS corresponds to N attempted swaps.

To model phase separation in the Fe–Cr system, it is necessary to match the phase diagram from the Monte Carlo simulations to the experimentally observed Fe–Cr miscibility gap. The miscibility gap in the b.c.c. region of the Fe–Cr phase diagram was first experimentally located by Williams and Paxton [1, 30], using hardness and electrical resistivity measurements. A critical temperature of ~830 K was found. Within this miscibility gap the only competing phase transformation is a sluggish sigma phase reaction [31]. The approximate form of the miscibility gap has been confirmed by other experimental studies, for instance Nishizawa *et al.* [32]. However Kuwano [33], using Mössbauer spectroscopy to follow the time development of the Cr-rich paramagnetic phase, reported a critical temperature (T_c) of ~950 K. The miscibility gap has also been located by thermodynamic calculations which include the magnetic transition.

Andersson and Sundman [34] predicted $T_c \approx 900$ K at a composition C_c of ~ 0.5. A summary of these experimental results and thermodynamic calculations is shown in Fig. 11. Also included in Fig. 11 are data from FIM observations. The closed circles represent experiments in which phase separation was observed and the open circles represent experiments in which no phase separation was observed.

To introduce a temperature into the Monte Carlo simulations, the critical temperature for an equiatomic simulation was set to 900 K. Since the critical energy parameter $(-\epsilon/kT_c)$ is known for each lattice [35], choosing a critical temperature fixes the corresponding value of the interaction parameter (ϵ). A good match is attained both with experimental results and thermodynamic calculations (Fig. 12).

The miscibility gap in the Fe–Cr system is not quite symmetrical and the Fe–45% Cr alloy produces a 50% volume fraction of each phase at 773 K. Since the miscibility gap defined by the Monte Carlo model is symmetric, simulations containing 50% A and 50% B atoms were chosen to model the real alloys. Simulations were performed on a b.c.c. grid ($80 \times 80 \times 80$ lattice units) with both first and second nearest neighbour interactions for times up to 10,000 MCS at a temperature of 750 K. Further simulations have also been performed on a range of different lattice types, lattice sizes and temperatures. During the "time scales" examined in this series of papers, the development of phase separation was not influenced by the simulation size.

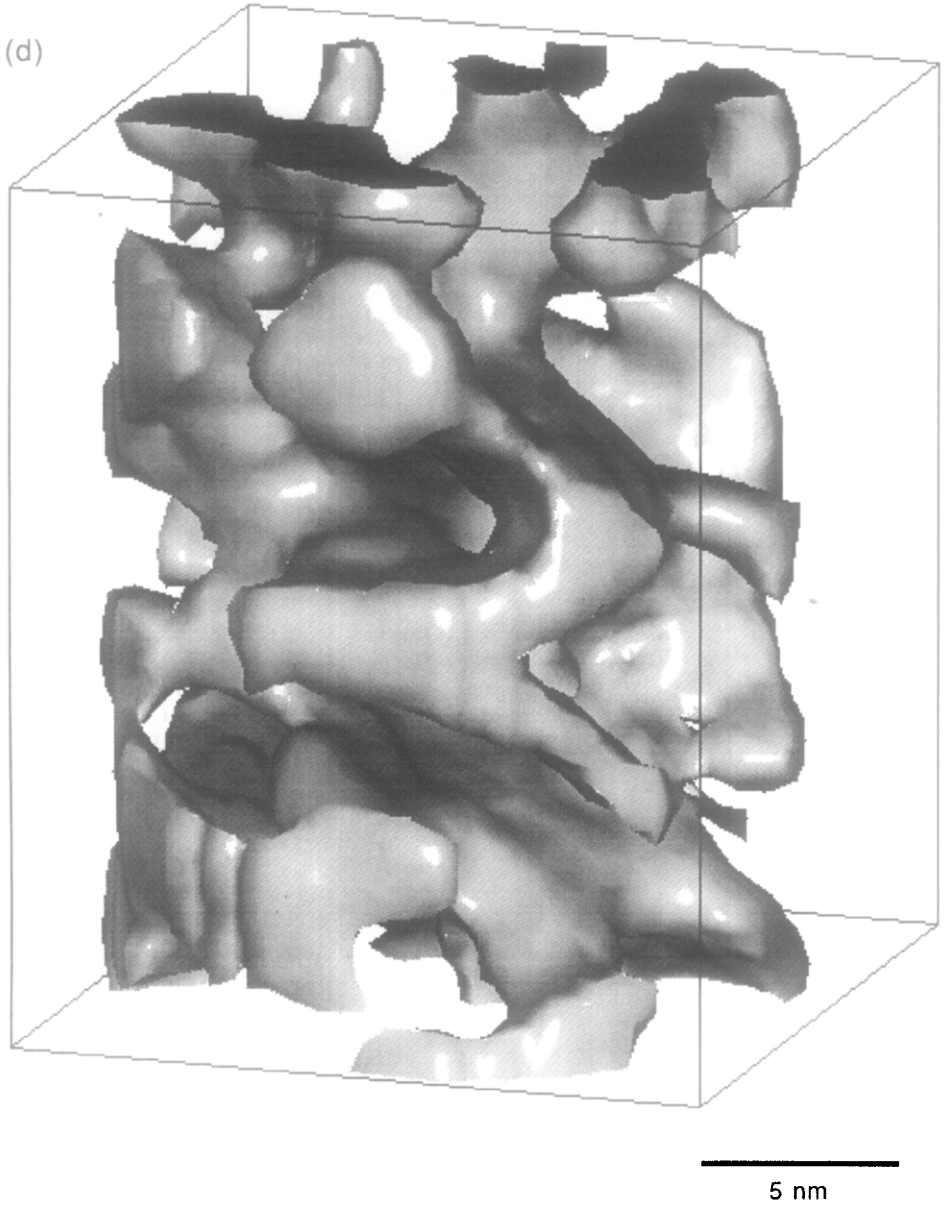

Fig. 10(d). (*Caption on p.* 3397.)

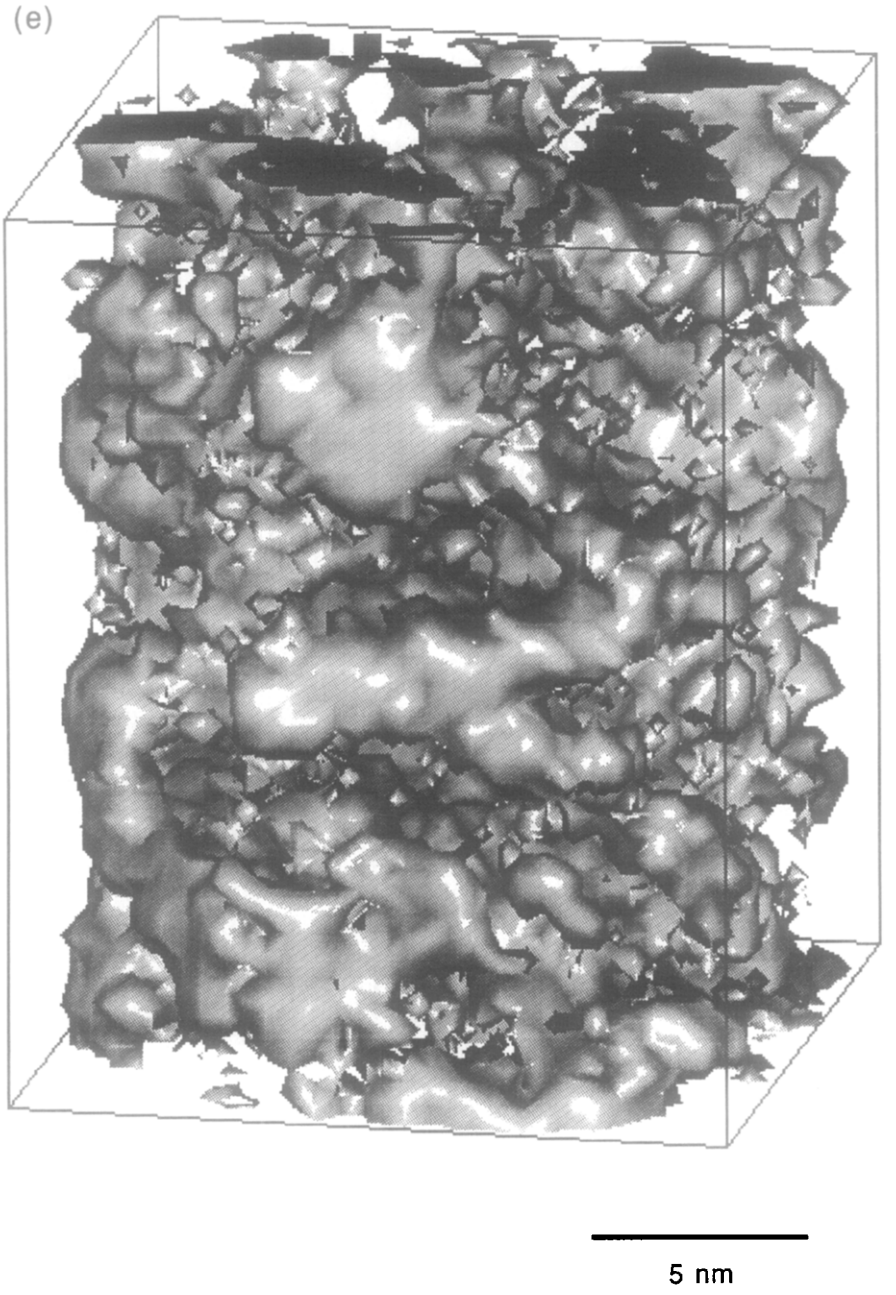

Fig. 10. Isosurface reconstructions from PoSAP analyses showing how the morphology of the Cr-enriched regions of Fe–Cr alloys varies as a function of Cr content after aging for 500 h at 773 K. The compositions are (a) Fe–17% Cr (isosurface at 20% Cr), (b) Fe–24% Cr (isosurface at 30% Cr), (c) Fe–32% Cr (isosurface at 30% Cr) and (d) Fe–45% Cr (isosurface at 40% Cr). In each simple smoothing has been used to generate the compositional information. In (e) centre-weighted smoothing was used to show the fine scale detail in an Fe–45% Cr alloy. The isosurface is drawn at a concentration of 40% Cr.

After aging for 5000 MCS at 750 K, the Ising model had produced a two-phase microstructure with a scale similar to that observed experimentally in the Fe–45% Cr alloys after aging for 500 h at 773 K. The isosurface reconstruction shown in Fig. 12, generated from a $40 \times 40 \times 40$ subsection of the Monte Carlo simulation, compares favourably with the PoSAP analysis [Fig. 10(e)]. The isosurface level was set to 50% in order to represent the interface between the phases. Both the Fe-rich and Cr-enriched phases are interconnected and percolate the volume.

4.3. Numerical solution to the Cahn–Hilliard–Cook theory

Cahn and Hilliard developed a mean field approach to spinodal decomposition of a binary mixture [23]. A local concentration variable u was defined in terms of the difference between the mole fractions of each

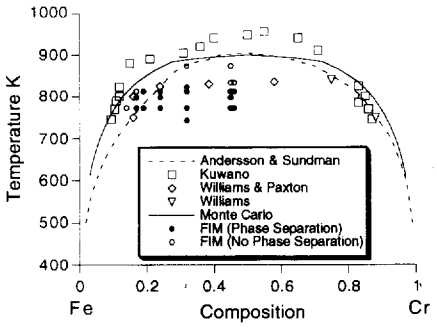

Fig. 11. The solid state miscibility gap in the Fe–Cr phase diagram. The dotted lines represent the thermodynamic calculations for the miscibility gap and the solid symbols are from experimental investigations. The phase diagram from the dynamic Ising model is shown with a critical temperature set to 900 K.

species, x and $(1-x)$, over a coarse-graining volume. The mole fraction within the coarse-graining region is

$$x(r) = \frac{1}{N}\sum_{i \in vol} x_i$$

where r is the centre of mass of the coarse grained volume containing N atoms and the x_i's are 0 and 1 corresponding to the two types of atoms. The continuous concentration parameter u is given by

$$u = x - (1-x) = 2x - 1, \quad |u| \leqslant 1.$$

The Ginzburg–Landau free energy function was used in which the chemical potential μ consists of two terms, relating to the bulk free energy, ψ, and a root mean square effective interaction distance γ. Both terms explicitly contain the coarse-grain scaling length through the definition of u

$$\mu = \frac{\partial \psi}{\partial u}(u) - \gamma^2 k_B T \nabla^2 u$$

where k_B is Boltzmann's constant and T is the temperature.

The Cahn–Hilliard equation for spinodal decomposition is

$$\frac{\partial u(r,t)}{\partial t} = \nabla \cdot M \nabla \left(\frac{\partial \psi}{\partial u}(u) - \gamma^2 k_B T \nabla^2 u \right)$$

where u is the composition, $M > 0$ a mobility, r is a position vector and t the time variable.

A major drawback of the Cahn–Hilliard theory is that it is completely deterministic and ignores thermal fluctuations. Cook [24] considered a simple extension to the linear theory by adding a random fluctuation $\xi(r,t)$

$$\frac{\partial u(r,t)}{\partial t} = \nabla \cdot M \nabla \left(\frac{\partial \psi}{\partial u}(u) - \gamma^2 k_B T \nabla^2 u \right) + \xi(r,t)$$

where

$$\langle \xi(r,t) \rangle = 0$$

and

$$\langle \xi(r,t)\xi(r',t') \rangle = -2k_B T M \nabla^2 \delta(r-r')\delta(t-t').$$

The two conditions ensure that the alloy composition is conserved and that the noise is uncorrelated in time. A convenient form of the Cook term is a Gaussian with mean zero and variance $2k_B TM$.

In the present work, a numerical solution to the non-linear Cahn–Hilliard equation, first implemented by Elliott and Copetti [36–38], was modified to include the Cook term. The parameters in the simulation were chosen in an attempt to model decomposition in the Fe–Cr system at 773 K. Since the experimental results correspond to the very early stages of decomposition, where the important length scales are on the order of a few atoms, an unrealistic coarse-grained volume of a single atom was chosen. The mean field approximation for the free energy, ψ, at a temperature of 750 K was used since the limits of solid solubility at this temperature approximately match those observed in the Fe–Cr system at 773 K. Positive compositions ($u > 0$) correspond to A-rich regions and negative compositions ($u < 0$) correspond to B-rich regions. If only nearest neighbour interactions are used, $\gamma = a/\sqrt{3}$ where a is the intermolecular distance [23]. The constant a^2/Mk_BT was absorbed into the definition of time so that one time unit is equal to a^2/Mk_BT seconds.

Simulations were performed on a cubic mesh ($64 \times 64 \times 64$) with a mean composition $u = 0$, corresponding to an equi-atomic alloy. Computational limitations prevented increasing the size of the simulations. Simulations were performed for values of $(\gamma/a)^2$ between 1/6 and 1 to model a range of interaction distances. Since the value of M at 750 K is not known, simulations were performed with a range of values for the magnitude of the Cook term. Simulations were performed until the mean distance between domains had reached at least 5 nm.

The evolution of the microstructure generated by the numerical discretization of the Cahn–Hilliard–Cook equation was analysed. In each simulation domain growth was observed after approx. 100 time units, generating a highly interconnected structure. After 1000 time units the scale was similar to that observed in the most heavily aged Fe–45% Cr alloy (500 h). In Fig. 13, an isosurface reconstruction (drawn at a composition of $u = 0$—the mean alloy composition) is shown which can be directly compared with the experimental results shown in Fig. 10(e) (each image is approx. 15 nm across). Although the scale is similar, the detailed morphology is different. The Cahn–Hilliard–Cook equation predicts smoother interfaces between the phases than the experimental results. The differences in morphology are discussed further in Part III of this series [19].

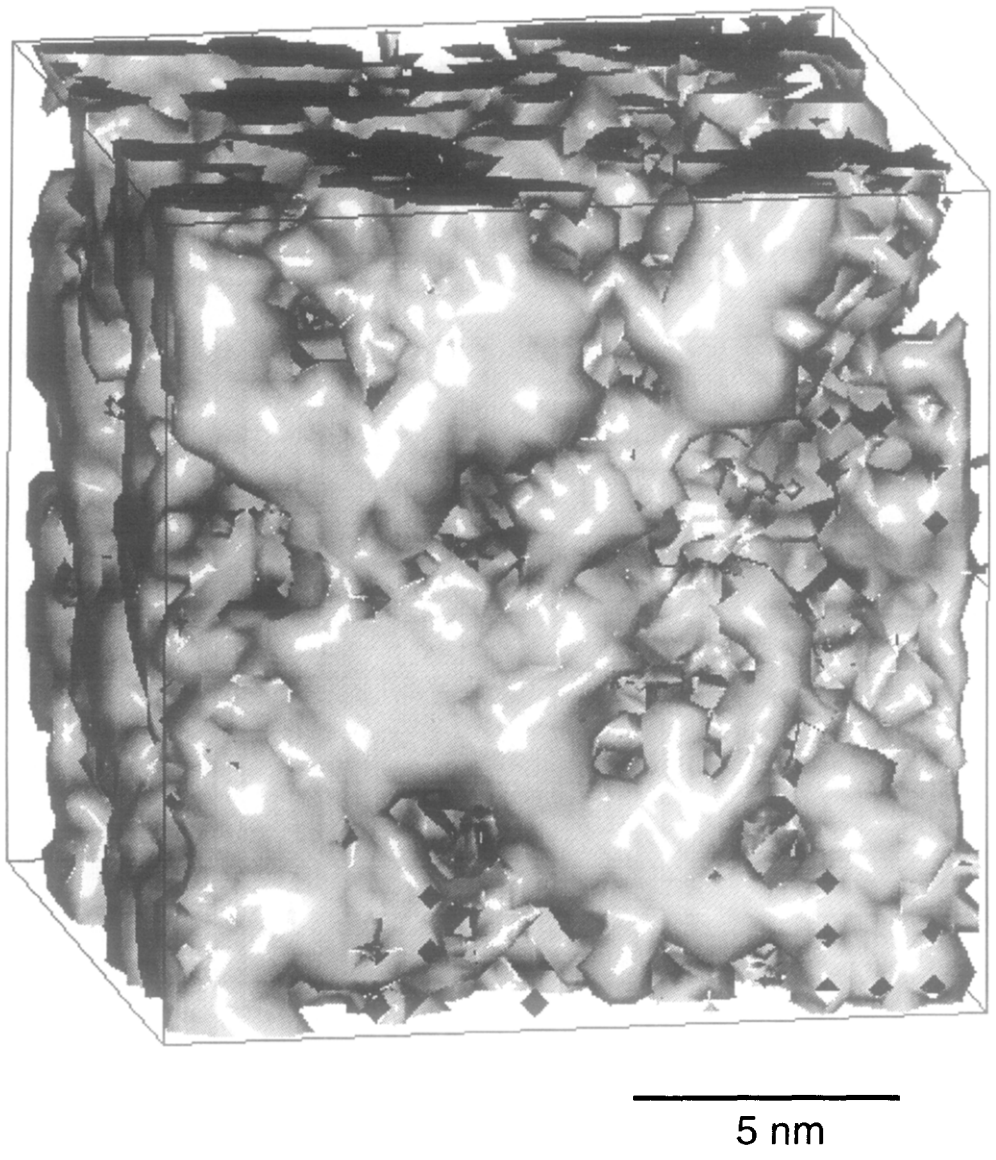

Fig. 12. Isosurface reconstruction of the B-rich regions from a Monte Carlo simulation on a body centred cubic lattice aged at 750 K for 5000 MCS. The compositions were calculated using centre-weighted smoothing and the surface is drawn at a concentration of 50 at.%.

5. MATCHING OF MODELS AND EXPERIMENT

In order to make a comprehensive comparison between experimental data and computer simulated results, the limitations of the experimental method must be taken into account. Extensive analyses have been performed on the position sensitive atom probe to ensure that the experiments were conducted under optimum conditions. However, a certain loss of data will always occur because the position sensitive detector cannot position more than one ion from any single pulse and the channel plates are not 100% efficient. Moreover, the trajectory aberrations and finite resolution of the position sensitive anode reduces the accuracy of the reconstructed atomic positions.

In the Monte Carlo model the exact position of each atom is known and so it is possible to model the experimental limitations and observe the effect on any measurements. The addition of a Gaussian scatter of width 1 atomic spacing to the lateral dimensions accurately models the trajectory aberrations and detector spatial resolution present during a typical PoSAP experiment [39]. The finite detection efficiency of the channel plates, coupled with the loss of position information from multiple events, reduces the detection efficiency of Cr atoms to 30%, and the detection efficiency of Fe atoms to 50% [21]. This reduces the apparent Cr-content of the alloy. To simulate this loss of data, a detection efficiency parameter, E_X, was introduced for each species X. A fraction $(1 - E_X)$ of the X type atoms are randomly

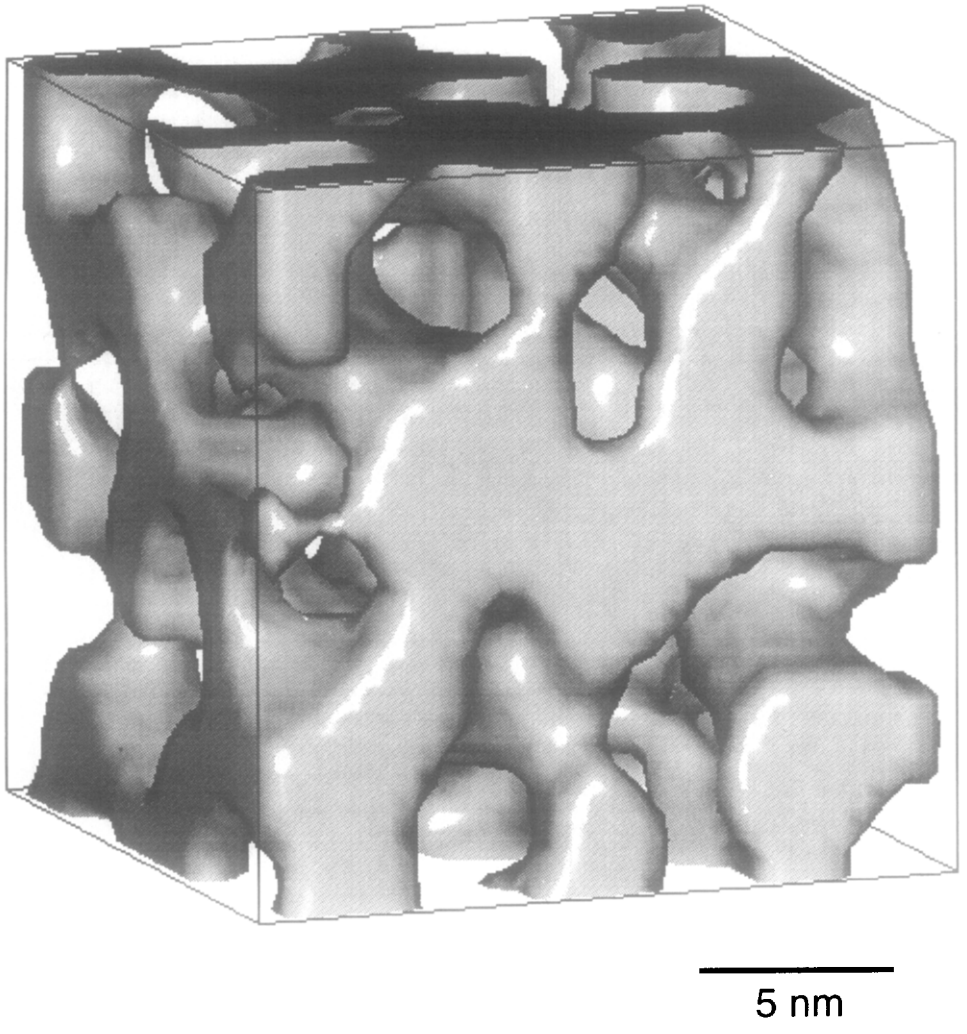

Fig. 13. Isosurface reconstruction of the B-rich regions from the numerical solution to the Cahn–Hilliard–Cook equation after aging for 1000 time units. The compositions were calculated using centre-weighted smoothing and the surface is drawn at a concentration of 50 at.%.

removed from the Monte Carlo simulation results prior to analysis. The effect of these experimental limitations on the observed compositions and morphology is discussed in detail in Parts II and III [18, 19].

6. CONCLUSIONS

Recent advances in atom probe microanalysis now enable the investigation of complex microstructures in 3D at the atomic level. The availability of computing power has led to the successful implementation of theoretical models which may be directly compared with the experimental results. The isosurface reconstructions from the position sensitive atom probe, Cahn–Hilliard–Cook model and Monte Carlo approach all generate structures that are qualitatively similar. A more quantitative comparison will be described in Parts II and III.

Acknowledgements—The authors would like to thank Professor R. J. Brook for the provision of laboratory facilities, Dr B. Fisher for supplying some of the alloys and Dr P. Camus who performed some of the early FIM experiments. J.M.H. would like to acknowledge the Engineering and Physical Sciences Research Council (EPSRC) and Wolfson College for financial support. A.C. thanks The Royal Society for financial support and Wolfson College for the provision of a Fellowship. This research was funded by the EPSRC under grant number GR/H/38485 and by the Division of Materials Sciences, U.S. Department of Energy, under contract DE-AC05-84OR21400 with Martin Marietta Energy Systems Inc. The simulations were performed in the Materials Modelling Laboratory at Oxford University which is funded by the EPSRC under grant number GR/H/58278.

REFERENCES

1. R. O. Williams, *Trans. AIME* **212,** 497 (1958).
2. M. J. Marcinkowski, R. J. Fisher and A. Szirmae, *Trans. Metall. Soc. AIME* **230,** 676 (1964).

3. S. S. Brenner, M. K. Miller and W. A. Soffa, *Scripta metall.* **16,** 831 (1982).
4. J. M. Hyde, A. Cerezo, M. G. Hetherington, M. K. Miller and G. D. W. Smith, *Surf. Sci.* **266,** 370 (1992).
5. J. C. LaSalle and L. H. Schwartz, *Decomposition of Alloys: The Early Stages* (edited by P. Haasen, V. Gerold, R. Wagner and M. Ashby), pp. 104 109. Pergamon Press, Oxford (1984).
6. J. C. LaSalle and L. H. Schwartz, *Acta metall.* **34,** 989 (1986).
7. M. Furusaka, Y. Ishikawa, S. Yamaguchi and Y. Fujino, *J. Phys. Soc. Japan* **55,** 2253 (1986).
8. F. Bley, *Acta metall. mater.* **40,** 1505 (1992).
9. K. A. Harwick, Ph.D. thesis, Edinburgh, Scotland (1991).
10. E. W. Müller, J. A. Panitz and S. B. McLane, *Rev. Sci. Instrum.* **39,** 83 (1968).
11. E. W. Müller and S. V. Krishnaswamy, *Rev. Sci. Instrum.* **45,** 1053 (1974).
12. A. Cerezo, T. J. Godfrey and G. D. W. Smith, *Rev. Sci. Instrum.* **59,** 862 (1988).
13. A. Cerezo, T. J. Godfrey and G. D. W. Smith, *J. Physique* **C6-49,** 25 (1988).
14. G. D. W. Smith and A. Cerezo, *Improvements in Atom Probes*. European Patent No. 0231247, granted 10th October (1990).
15. M. K. Miller, *Surf. Sci.* **246,** 428 (1991).
16. M. K. Miller, *Surf. Sci.* **266,** 494 (1992).
17. M. K. Miller and G. D. W. Smith, *Atom-Probe Microanalysis: Principles and Applications in Materials Science*. Materials Research Society, Pittsburgh, Pa (1989).
18. J. M. Hyde, M. K. Miller, M. G. Hetherington, A. Cerezo, G. D. W. Smith and C. M. Elliott, *Acta metall. mater.* **43,** 3403 (1995).
19. J. M. Hyde, M. K. Miller, M. G. Hetherington, A. Cerezo, G. D. W. Smith and C. M. Elliott, *Acta metall. mater.* **43,** 3415 (1995).
20. M. K. Miller, *J. Phys. (Paris)* **47,** 493 (1986).
21. A. Cerezo, J. M. Hyde, M. K. Miller, G. Beverini, R. P. Setna, P. J. Warren and G. D. W. Smith, *Surf. Sci.* **266** (1992) 481.
22. J. W. Cahn, *Acta metall.* **9,** 795 (1961).
23. J. W. Cahn and J. E. Hilliard, *J. chem. Phys.* **28,** 258 (1958).
24. H. E. Cook, *Acta metall.* **18,** 297 (1970).
25. J. S. Langer, M. Bar-on and H. D. Miller, *Phys. Rev. A* **11,** 1417 (1975).
26. M. Grant, M. S. Miguel, J. Viñals and J. D. Gunton, *Phys. Rev. B* **31,** 3027 (1985).
27. N. Metropolis, A. W. Rosenbluth, M. N. Rosenbluth and A. H. Teller, *J. chem. Phys.* **21,** 1087 (1953).
28. K. Yaldram and K. Binder, *Z. Phys. B—Condensed Matter* **82,** 405 (1991).
29. V. Heine, *Phys. Rev.* **153,** 673 (1967).
30. R. O. Williams and H. W. Paxton, *J. Iron Steel Inst.* **185,** 358 (1957).
31. W. C. Leslie, *The Physical Metallurgy of Steels* (edited by D. Hieberg, V. M. Ziobro and E. Dugger), pp. 337–340. McGraw-Hill, New York (1982).
32. T. Nishizawa, M. Hasebe and M. Ko, *Acta metall.* **27,** 817 (1979).
33. H. Kuwano, *Trans. Japan Inst. Metals* **26,** 473 (1985).
34. J. Andersson and B. Sundman, *CALPHAD* **11,** 83 (1987).
35. G. A. Baker, *Phys. Rev.* **124,** 768 (1961).
36. C. M. Elliott and D. A. French, *IMA J. appl. Math.* **38,** 97 (1987).
37. C. M. Elliott, *Int. Ser. Num. Math.* **88,** 35 (1989).
38. M. I. M. Copetti and C. M. Elliott, *Mater. Sci. Technol.* **6,** 273 (1990).
39. J. M. Hyde, D.Phil. thesis, University of Oxford (1993).